Modeling TEC Irregularities in the Northern Hemisphere Using Empirical Orthogonal Function Method

Yaqi Jin[1*], Wojciech J. Miloch[1], Daria Kotova[1], Knut Stanley Jacobsen[2], Đorđe Stevanovic[3], Lasse B. N. Clausen[1], Nicholas Ssessanga[1], and Federico Da Dalt[4]

[1]Department of Physics, University of Oslo, P.O. Box 1048 Blindern, 0316 Oslo, Norway

[2]Norwegian Mapping Authority, PO 600 Sentrum, 3507 Hønefoss, Norway

[3]GMV Innovating Solutions, Warsaw, Poland

[4]Rhea System GmbH, Darmstadt, Germany

[*]Corresponding author: Yaqi Jin (yaqi.jin@fys.uio.no)

Short title: **Modeling of ROTI maps**

Key Points

1. An empirical model of ROTI maps in the Arctic is developed based on 12 years of ROTI data using the EOF method
2. The statistical data-model comparisons show satisfactory results
3. The model fails to capture the significant expansion of the dayside ROTI activity during severe geomagnetic storms

Abstract

We develop a climatological model for the Northern Hemisphere based on a long-term dataset (2010-2021) of the rate of change of the total electron content (TEC) index (ROTI) maps from the International GNSS Service (IGS). The IGS ROTI maps are daily averaged in magnetic latitude and local time coordinates. To develop a climatological model, the ROTI maps are decomposed into a few base functions and coefficients using the empirical orthogonal function (EOF) method. The EOF method converges very quickly, and the first four EOFs reflect the majority (96%) of the total data variability. Furthermore, different EOF components can reflect different drivers of ionospheric irregularities. The first EOF reflects the averaged ROTI activity and the impact of the solar radiation and geomagnetic activity; the 2nd EOF reflects the impact of the interplanetary magnetic field (IMF) Bz and electric field; the 3rd and 4th EOFs reflect the dawn-dusk asymmetry around the auroral oval and polar cap, and they can be related to the IMF By. To build an empirical model, we fit the EOF coefficients using helio-geophysical indices from four different categories (solar activity; geomagnetic indices; IMF; the solar wind coupling function). The final EOF model is dependent on seven selected indices (F10.7P, Kp, Dst, Bt, By, Bz and E_{kl}). The statistical data-model comparisons show satisfactory results with a good correlation coefficient. However, the model cannot capture the significant expansion of the dayside ROTI activity during strong geomagnetic storms. Future effort is needed to provide corrections to the model during severe storms.

Plain Language Summary

The ionosphere is often highly structured and contains significant irregularities of plasma density, which can impact the Global Navigation Satellite System (GNSS) services that rely on trans-ionospheric radio waves. Due to the practical use of GNSS services, there is a high demand for modeling and forecasting of ionospheric irregularities. In this study, we develop a climatological model for the Northern Hemisphere based on a long-term dataset from the International GNSS Service (IGS). The final model is dependent on a few helio-geophysical indices that represent the main drivers/sources of ionospheric irregularities. The statistical data-model comparisons show that the model is able to reproduce all the climatological features of ionospheric irregularities. This model can be useful in forecasting the space weather impact for GNSS users using real-time data as input.

1 Introduction

Ionospheric irregularities and scintillations have received more and more attention due to the increasing number of Global Navigation Satellite System (GNSS) users. The GNSS service can be heavily degraded due to space weather phenomena (Basu et al., 2002; Kintner et al., 2007; Jakowski et al., 2012). To enable forecasting and mitigation of the adverse space weather effects, it is essential to model ionospheric irregularities and scintillations (Wernik et al., 2007; Secan et al., 1997; Priyadarshi, 2015; McGranaghan et al., 2018).

Ionospheric irregularities have been investigated using in-situ techniques (e.g., Basu et al., 1990; Coley & Heelis, 1998; Moen et al., 2012; Jin et al., 2022b) and ground-based instruments (e.g., Rino et al., 1983; Tsunoda, 1988). With the advent of GNSS, ground-based GNSS receivers have been widely used to monitor and study ionospheric irregularities. Many researchers use amplitude and phase scintillation indices based on the high-resolution measurements from specialized GNSS scintillation receivers (Van Dierendonck et al., 1993; Mitchell et al., 2005; Spogli et al., 2009; Jin et al., 2019a), while others focus on the rate of change of total electron content (TEC) index (ROTI) as a measure of ionospheric irregularities (Pi et al., 1997; Basu et al., 1999). The advantage of ROTI is that it can be obtained from any geodetic receivers (normally from dual-frequency measurements). Therefore, the global extent and long-term variability of ionospheric irregularities can be investigated using global networks of GNSS stations (e.g., Cherniak et al., 2014, 2018a; Jacobsen & Dahnn, 2014; Jacobsen, 2014; Kotulak et al., 2020). More recently, daily ROTI maps in the northern mid- and high-latitude regions have been developed by using GNSS data from about 700 selected permanent stations (Cherniak et al., 2014; Cherniak et al., 2018b) The ROTI maps are provided to the International GNSS Service (IGS) and are openly available for scientific purposes. The newly available ROTI maps provide continuous information about the quiet-time background ionospheric irregularities as well as intense ionospheric variability during storms (Cherniak et al., 2018b). Therefore, the IGS ROTI maps provide a valuable dataset for developing a data-driven empirical model of ionospheric irregularities.

In order to forecast ionospheric irregularities and scintillations, different approaches have been used. The climatological models of ionospheric irregularities and scintillation have been widely used. For example, the WBMOD (WideBand MODel) ionospheric scintillation model is the most popular climatological model that was first developed in the 1970s and upgraded later on (Secan et al., 1997). Wernik et al. (2007) established a method to model scintillation effect using in-situ ionospheric density data from Dynamics Explorer 2 satellite. A comprehensive review of existing climatological models of ionospheric scintillation can be found in Priyadarshi (2015). More recently, Fabbro et al. (2021) established a model of ROTI and GNSS positioning error by parameterization of the solar wind

measurements. Jin et al. (2022a) developed an empirical ROTI model based on GNSS data over two solar cycles in Greenland using the Empirical Orthogonal Function (EOF) method. The latter model only depends on F10.7P, Interplanetary Magnetic Field (IMF) Bt and Dst index. Despite its simplicity, the model gives very satisfactory results with a high correlation coefficient. In the present paper, we extend the 1-D ROTI model, and establish a 2-D ROTI model by using the IGS ROTI maps over one solar cycle (2010-2021).

2 Dataset

2.1 ROTI maps

We make use of daily ROTI maps from the International GNSS Service (IGS) (Cherniak et al., 2014; Cherniak et al., 2018b). ROTI is defined as the standard deviation of rate of change of TEC (ROT) in 5 minutes, where ROT is the time derivative of TEC (Pi et al., 1997). Both ROT and ROTI are in units of TECU/min. To construct the ROTI maps, Cherniak et al. (2018b) collected Receiver Independent Exchange (RINEX) format data with a 30-s sampling rate from about 700 GPS stations located at high and middle latitudes in the Northern Hemisphere. The final product is presented as daily maps in coordinates of magnetic latitude (MLAT) and magnetic local time (MLT). Each map starts from 50° MLAT with a spatial resolution of 2° in MLAT and 2° in longitude (8 minutes in MLT). Although the ROTI maps are from mid- to high latitudes, we focus on high latitudes in this present study. For more detail about the methodology, please refer to Cherniak et al. (2014) and Cherniak et al. (2018b). Figure 1 presents an example of ROTI maps during November 1 - 15, 2021. To assist eyes, the Feldstein auroral oval (Q = 3) (Holzworth & Meng, 1975) is shown by magenta curves. The spatial distribution of ROTI activity is generally guided by the auroral oval, where enhanced ROTI often occurs around the auroral oval, and inside the polar cap (poleward of the auroral oval). Note that there was a magnetic storm during November 3-5, 2021 that started at around 21 UT on November 3. The daily ROTI map captures well the storm conditions, which are reflected as enhanced ROTI values and expanded area of significant ROTI activity on November 4. The ROTI maps are available from January 2010 to November 2022 through the ftp server of NASA's Crustal Dynamics Data Information System (CDDIS) ftp://cddis.gsfc.nasa.gov/pub/gps/products/ionex (accessed in April 2023). In this study, we use ROTI maps from 2010 to 2021 to develop the EOF model, while the data in 2022 are used only for the purpose of validation.

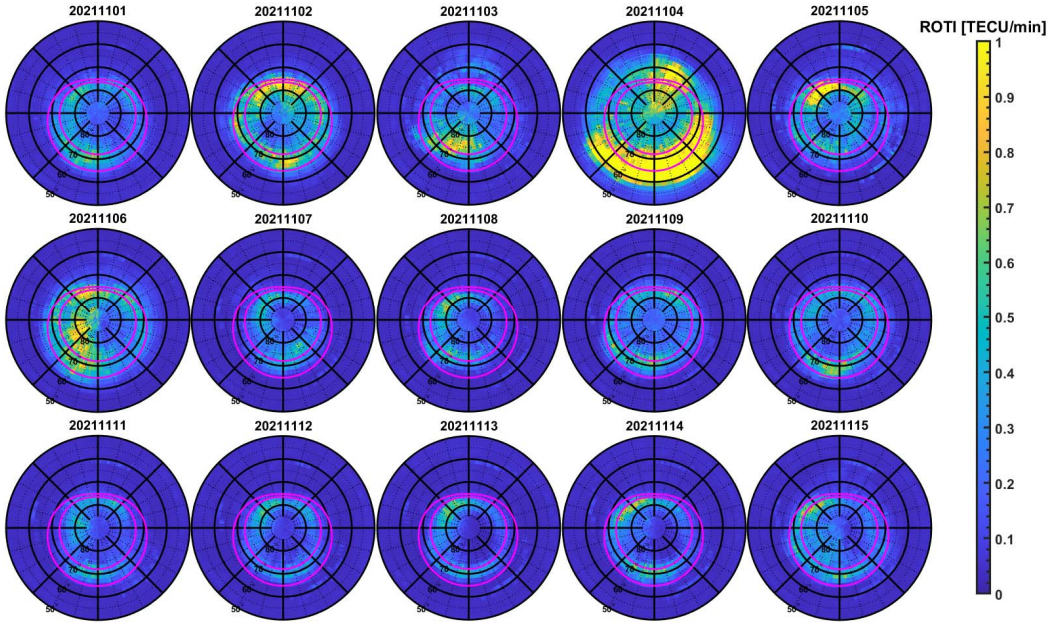

Figure 1. Example of the IGS ROTI maps during November 1 - 15, 2021. The ROTI maps are presented in MLAT/MLT coordinates starting from 50° MLAT. In each panel, noon is to the top, and dawn is to the right. The Feldstein auroral oval (Q = 3) is shown by magenta curves to guide the analysis. Note that one major geomagnetic storm (Dst reached -105 nT) occurred during November 3-5, 2021.

2.2 Helio-geophysical proxies

The high-latitude ionosphere is directly driven by the solar activity, solar wind, and magnetospheric phenomena. We use different solar and geophysical indices to represent these drivers. We use four general classes of helio-geophysical proxies that characterize the space environment: 1) the solar activity (F10.7, sunspot number etc.), 2) geomagnetic indices (Dst, Kp, ap etc.), 3) the IMF and solar wind conditions (IMF Bt, Bx, By, Bz, the solar wind speed Vsw, solar wind density and pressure), 4) interplanetary electric field (IEF) (IEF Ey, E_{kl}) and the Newell coupling function.

The F10.7 index measures the total emission of the solar disk at the wavelength of 10.7 cm, and it is widely used to represent the solar activity (e.g., Tapping, 2013). Due to its simplicity, the F10.7 index is often used to model the ionosphere (Bilitza et al., 2011). To represent the solar activity, there are also variations of the F10.7 index. For example, F10.7_81 is an average of the F10.7 solar flux index in a running window of 81 days (i.e., 3 solar rotations), while F10.7P is defined as (F10.7 + F10.7_81)/2 (Liu et al., 2011; Rentz & Lühr, 2008; Xiong et al., 2010). Liu et al. (2011) recommended using F10.7P for the common use of proxy of the solar activity. We have compared F10.7, F10.7_81, F10.7P and the sunspot number in our modeling work, and F10.7P turns out to be the best proxy for our purpose.

For the geomagnetic indices, we choose to use Kp, ap and Dst (Disturbance Storm Time) index. Kp index is a three-hourly geomagnetic index in quasi-logarithm scale that is derived from the standardized K index (Ks) of 13 worldwide observatories. It is designed to measure the solar particle radiation, and it is considered as a proxy for the energy input from the solar wind to Earth. More details about the Kp index can be found on the official Kp index webpage (https://www.gfz-potsdam.de/en/kp-index/). The 3-hourly ap (equivalent range) index can be derived from the Kp index using a table from https://www.ngdc.noaa.gov/stp/geomag/kp_ap.html. The Dst index is an hourly geomagnetic index that measures the intensity of the globally symmetrical equatorial electrojet (the "ring current") and is derived from four magnetic observatories at low latitudes. The variations of Dst provide quantitative information of the level of geomagnetic disturbances. The original Dst index can be downloaded from the World Data Center for Geomagnetism, Kyoto (http://wdc.kugi.kyoto-u.ac.jp/dstdir/). For the present study, we use the daily averaged Kp, ap and Dst indices from the NASA CDAWeb (https://cdaweb.gsfc.nasa.gov/index.html/).

The upstream solar wind speed, solar wind dynamic pressure, IMF, and IEF are obtained from the daily averaged OMNI dataset (King & Papitashvili, 2005). In addition, we also use the Kan-Lee electric field ($\mathrm{E_{KL}} = \mathrm{V} \cdot \mathrm{B}_t \cdot \sin^2 \theta_c$, where V is the solar wind speed, B_t is the IMF strength, and θ_c is the IMF clock angle) and the Newell coupling function ($d\Phi_{MP}/dt = V^{4/3} B_t^{2/3} \sin^{8/3}(\theta_c/2)$) to account for the solar wind-magnetosphere-ionosphere coupling (Kan & Lee, 1979; Newell et al., 2007). The clock angle (θ_c) is defined as the angle between the Z-axis and the projection of the IMF vector onto the Y-Z plane of the geocentric solar magnetospheric (GSM) coordinate system.

3 Results

3.1 Climatology of ROTI maps

We first present the general climatology of ROTI maps at high latitudes. It has been shown that ionospheric irregularities strongly depend on solar activity (Basu et al., 1988; Jin et al., 2018; De Franceschi et al., 2019). Figure 2 shows the yearly averaged ROTI maps from 2010 to 2022. The yearly averaged F10.7 index is also annotated on the top right of each panel. One can clearly observe solar activity dependence of the global ROTI maps, i.e., the ROTI values increase from 2010 near solar minimum to 2014 in solar maximum, then they decrease until 2019 followed by a slight increase of ROTI in the new solar cycle 25 (from 2020). Besides the solar activity dependence, the distribution of high ROTI values in each year is very similar. The averaged and standard deviation of ROTI maps are shown on the last two panels in Figure 2. There are two regions of high ROTI, i.e., the dayside hotspot around 75°-80° MLAT and 9-15 MLT, and the nightside hotspot around 68°-74° MLAT and 22-01 MLT. The spatial distribution is similar to previous studies of ionospheric irregularities using regional ROTI

data (Jacobsen, 2014), ionospheric scintillation data (Spogli et al., 2009; Jin et al., 2015), and in-situ measurements (Jin et al., 2019b; Jin et al., 2021).

To present the seasonal variations, Figure 3 shows the averaged ROTI maps for two seasons using the data from 2010 to 2022. The summer months are averaged using data from May, June, and July, while the winter months are averaged over November, December, and January. Clear seasonal variations can be observed, i.e., the ROTI values are higher and more extended during winter.

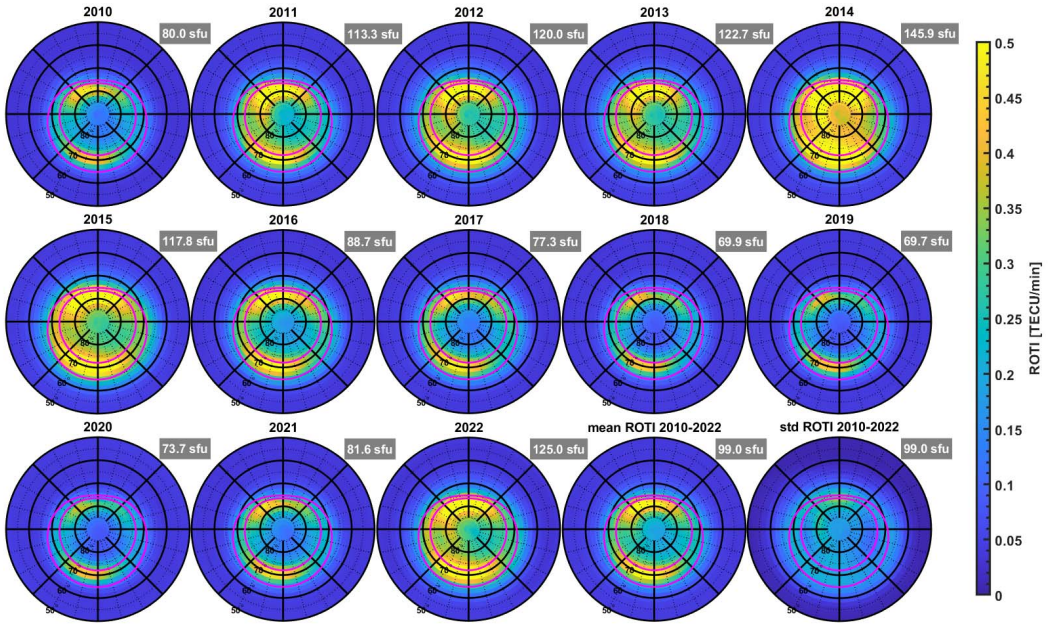

Figure 2. The yearly averaged ROTI maps in 2010-2022. Note that only 11 months of ROTI data is available in 2022. The last two panels show the mean and standard deviation (std) of ROTI over 2010-2022. The averaged F10.7 index for each time period is shown on the top right of each panel. The Feldstein auroral oval (Q = 3) is shown by magenta curves to guide the analysis. Clear solar activity dependence is observed.

Next, we present the temporal variations of ROTI activity in terms of season and solar cycle. Figure 4a shows the F10.7P index (red) and sunspot number (black). The solar cycle 23 starts in December 2008 and ends in December 2019. However, the IGS ROTI maps start from 2010. Therefore, only ROTI data from 2010 are presented in this paper. Clearly, the F10.7P index and sunspot number are high during solar maximum near 2014 and low during 2019-2020 near solar minimum. For example, the sunspot number reaches zero at the end of 2019. The solar activity greatly affects the climatological features of ROTI as shown in Figures 4b-4c. Figure 4b shows the ROTI climatology using MLT and day of year. To construct the statistics, the data are averaged along the MLAT from 50° to 90° at each fixed MLT. This is similar to the study by Jin et al. (2022a), where only a single GNSS station was used, while the

present paper uses IGS ROTI maps that are based on global networks of about 700 GNSS stations. The most remarkable variations of ROTI are associated with solar activity. During high solar activity years (2014-2015), the ROTI values are significantly enhanced. Besides, the averaged ROTI also shows clear seasonal variations, i.e., they are enhanced during equinox and winter seasons. In addition, ROTI shows diurnal variations, i.e., it varies as a function of MLT. ROTI increases from MLT noon and remains enhanced until midnight. During high solar activity years (e.g., the winter of 2014-2015), ROTI can remain enhanced all day.

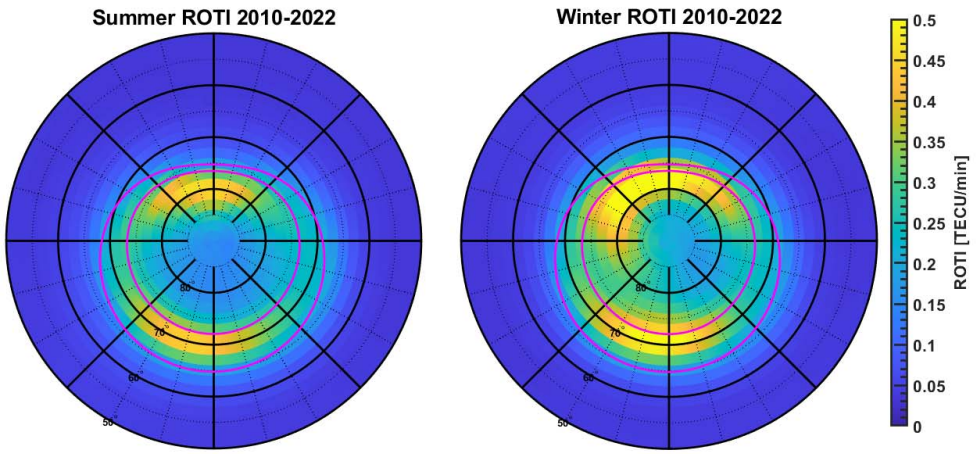

Figure 3. The averaged ROTI map for summer (May, June and July) and winter (November, December and January) months in 2010-2022.

Figure 4c shows the "keogram" format of ROTI data that is scanned along the noon-midnight meridian. The data are averaged over fixed MLT (11-13 MLT on the dayside and 23-01 MLT on the nightside). There are two bands of persistent ROTI enhancement both on the dayside and the nightside. On the dayside, the enhancement locates around 75˚-80˚ MLAT, while on the nightside, it is located around 68˚-74° MLAT. These two bands are associated with the cusp and nightside auroral dynamics respectively, and they are consistent with the spatial distribution of ROTI as shown in Figure 2. Though the dayside and nightside bands of ROTI enhancement are almost permanent, their intensity is dependent on the solar activity, such as they are more enhanced in 2012-2015. The central polar cap is between the two bands of ROTI enhancements. The central polar cap can be filled with enhanced ROTI during disturbed periods. For example, plasma structures can be associated with polar cap patches or tongue of ionization (TOI) (Foster et al., 2005; Zhang et al., 2015; Jin et al., 2014; van der Meeren et al., 2014). This phenomenon is dependent on the IMF orientations and geomagnetic activity, and they are more prevalent during high solar activity (Spicher et al., 2017).

Another interesting feature is the periodic variations of ROTI along MLAT around noon, i.e., high ROTI is located at the lowest MLAT in winter, and it drifts to the highest MLAT in summer. This feature is similar to the latitudinal variations of GPS phase scintillations (Jin et al., 2018). This phenomenon has been explained by the seasonal motion of the cusp location and the impact of the solar terminator (Jin et al., 2018; Newell & Meng, 1989).

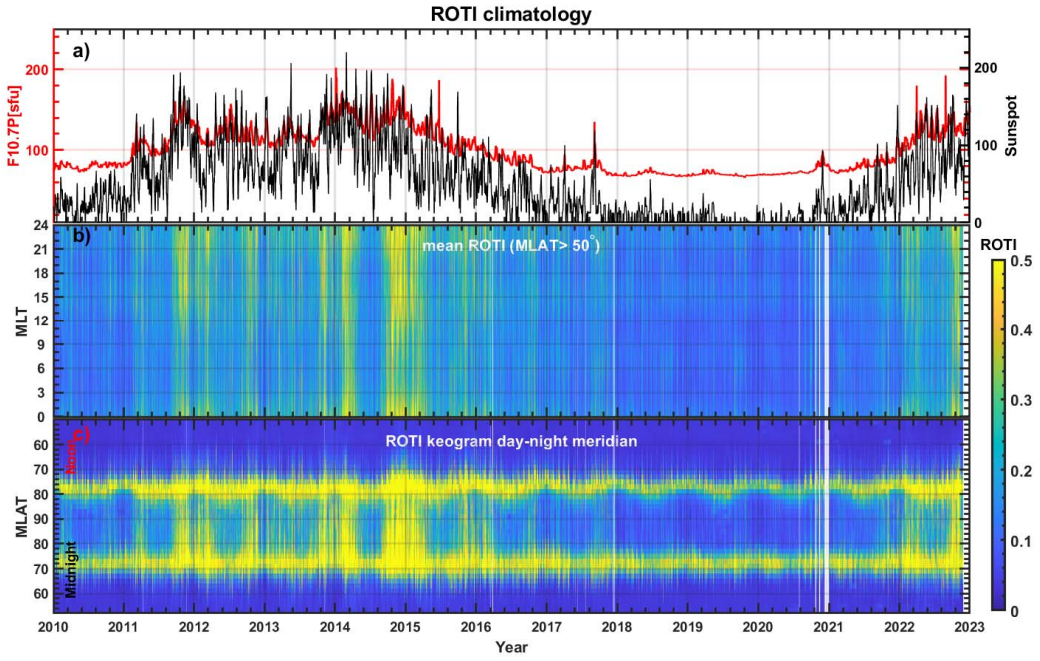

Figure 4. (a) The F10.7P solar flux index (red) and sunspot number (black). (b) The averaged ROTI over all MLAT (50°-90°). The data are presented in bins of 0.13 hour in MLT and 1 day. (c) The averaged ROTI along MLAT around magnetic noon (11-13 MLT) and magnetic midnight (23-01 MLT). The data are presented as a function of MLAT from the dayside (top) to the nightside (bottom). Note that some data are missing at the end of 2020.

3.2 EOF decomposition

Since the IGS ROTI maps are daily maps in geomagnetic coordinates, the ionospheric condition at each day can be expressed as $ROTI(MLAT, MLT, D)$. We use data during 2010-2021 (12 years) to account for the variations of time scales over one solar cycle. The EOF method is used to decompose the 3-D matrix into a series of EOF base maps and coefficients as follows:

$$ROTI(MLAT, MLT, D) = \sum_{i=1}^{4} E_i(\mathrm{MLAT}, \mathrm{MLT}) \times A_i(D) \quad (1)$$

Where $E_i(\mathrm{MLAT}, \mathrm{MLT})$ is the i-th EOF base function, and A_i is the i-th EOF coefficient. To keep simplicity, we only use the first four EOFs to reconstruct the ROTI maps. This is feasible as the EOF

228 method converges very quickly and the first few EOFs dominate the total variability (Dvinskikh &
229 Naidenova, 1991; Zhang et al., 2009; A et al., 2011; A et al., 2012; Jin et al., 2022a). Table 1 presents
230 the percentage of total ROTI variability captured by the first four EOFs. The first four orders of EOFs
231 contribute to 96.32% of the total data variability. Therefore, it is adequate to use the first four orders
232 of EOFs to build the climatological model.

233 Figure 5 shows the first four decomposed EOF coefficients, while Figure 6 shows the corresponding
234 EOF base functions. The correlation of the EOF coefficients with various helio-geophysical indices is
235 presented in Table 2. The first EOF component represents the average behavior of the ROTI maps. To
236 justify this statement, we plot the daily averaged ROTI as a red line in Figure 5a. A good
237 correspondence between A_1 and daily mean ROTI is observed. In addition, this point can be
238 confirmed from the first base function in Figure 6a, where the distribution of E_1 resembles the
239 averaged ROTI maps in Figure 2. The second EOF component is mainly controlled by the geomagnetic
240 activity and IMF Bz. Figure 6b shows an enhancement of E_2 from pre-noon to pre-midnight around 80°
241 MLAT and a depletion equatorward of the statistical auroral oval. Table 2 shows that the correlation
242 with the IMF Bz is high and positive (R=0.61). When the IMF Bz is positive, there should be an
243 enhanced ROTI around 80° MLAT from noon to dusk. This corresponds to a contracted auroral oval
244 during northward IMF Bz. When the IMF Bz is negative, there should be a ring of enhanced ROTI
245 equatorward of the Feldstein auroral oval. This corresponds to the expanded auroral oval during
246 negative IMF Bz due to dayside reconnection (Lockwood et al., 1990; Cowley & Lockwood, 1992). The
247 3^{rd} and 4^{th} EOF base functions show a clear dawn-dusk asymmetry. This indicates that the 3^{rd} and 4^{th}
248 EOF components represent the dawn-dusk asymmetry that is mainly controlled by the IMF By. A
249 close look at Table 2 confirms that the 3^{rd} and 4^{th} EOF coefficients indeed correlate with the IMF By.

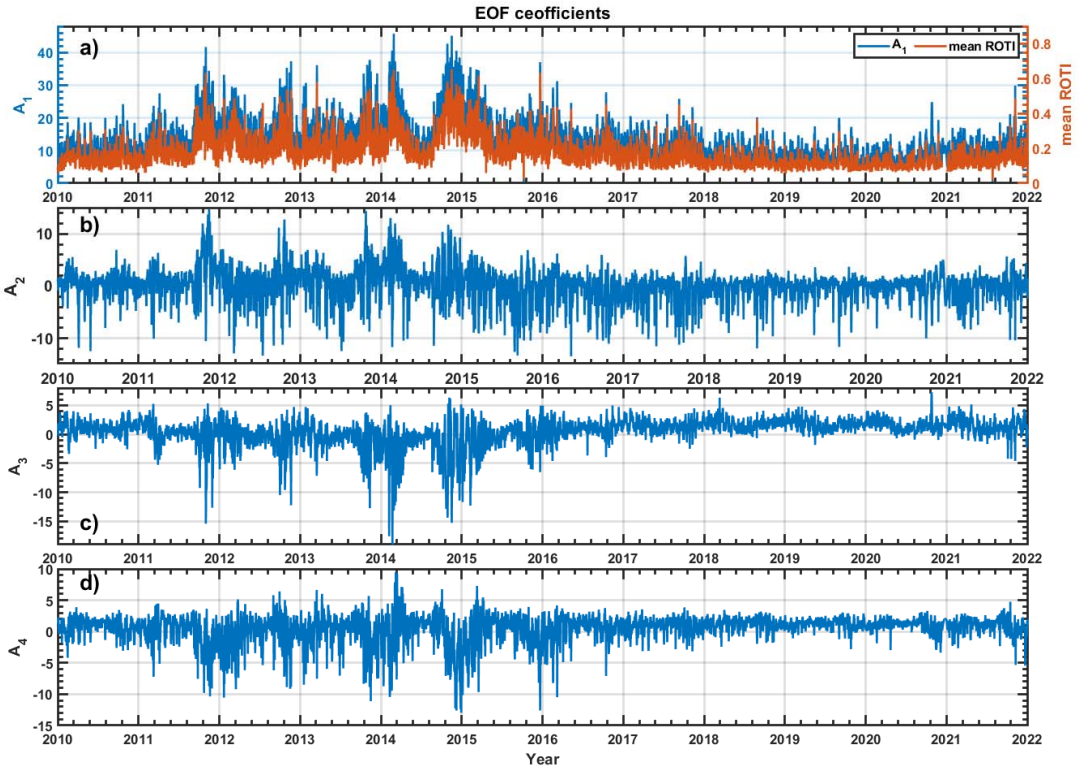

Figure 5. The first four decomposed EOF coefficients. The mean ROTI that is averaged over all MLAT and MLT in each day is displayed as red line in panel a).

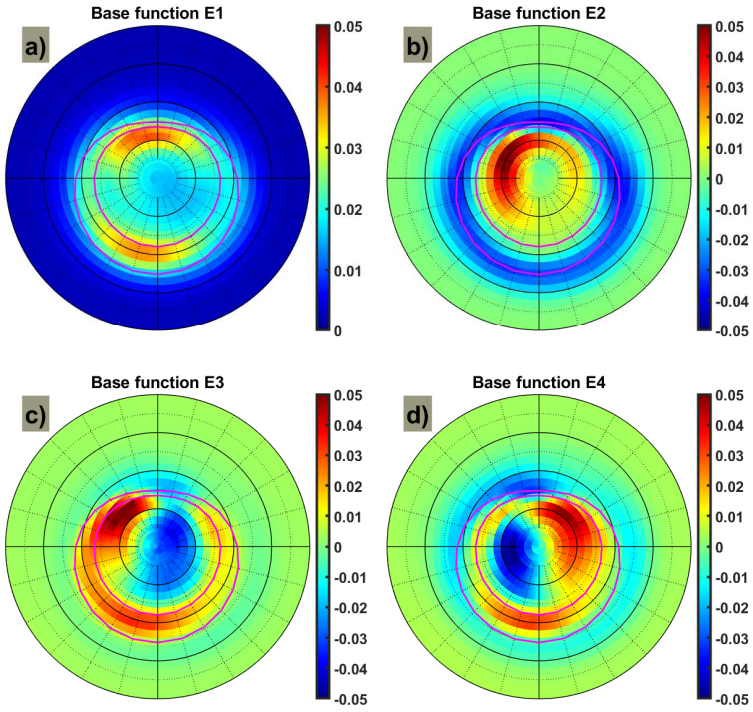

Figure 6. The first four decomposed EOF base functions.

Table 1. The percentage of data variability captured by the first four Empirical Orthogonal Functions (EOFs)

EOF	1	2	3	4
Percentage of Variability	87.30	4.43	2.42	2.16
Cumulative Percentage of Variability	87.30	91.73	94.16	96.32

Table 2. Correlation coefficients of the commonly used solar and geomagnetic indices with the first four EOF coefficients.

Coeff	A1	A2	A3	A4
F10.7P index	**0.65**	**0.25**	**-0.55**	**-0.30**
Sunspot Number	0.56	0.21	-0.45	-0.26
Kp index	**0.61**	**-0.71**	-0.04	**-0.29**
Dst index	-0.51	0.57	**0.15**	0.29
ap index	0.53	-0.68	-0.08	-0.33
IMF Bt	**0.58**	-0.30	-0.14	-0.34
IMF B_X	-0.00	0.09	0.31	-0.31
IMF B_Y (GSM)	0.04	-0.14	**-0.43**	**0.41**
IMF B_Z (GSM)	-0.19	**0.61**	-0.00	0.17
Solar Wind Speed	0.05	-0.09	0.07	-0.11
Solar Wind Pressure	0.33	-0.39	0.07	-0.09
IEF Ey	0.19	-0.62	-0.00	-0.19
Newell Coupling Function	0.45	-0.71	-0.03	-0.29
E_{k1}	**0.53**	**-0.71**	**-0.06**	**-0.35**

The next step is to fit the EOF coefficients by different classes of helio-geophysical indices. We use 4 general categories of helio-geophysical indices: 1) the solar activity (F10.7, sunspot number etc.), 2) geomagnetic indices (Dst, Kp, ap etc.), 3) solar wind and IMF components (solar wind speed Vsw, solar wind density, IMF Bt, Bx, By, Bz), 4) IEF and related indices (IEF, E_{kl}, the Newell coupling function). To ensure the simplicity and robustness of the model, we only select one, the most representative index in each category. This selection is mainly based on correlation analysis with the EOF coefficients as shown in Table 2. The selected indices are shown in bold font.

We use the following equations to fit the EOF coefficients A_i:

$$A_i(d) = B_{i1}(d) + B_{i2}(d) + B_{i3}(d) \quad (2)$$

$$B_{i1}(d) = C_{i1} + D_{i1} \times P_1(d) + E_{i1} \times P_2(d) + F_{i1} \times P_3(d) + G_{i1} \times P_4(d) \quad (3)$$

$$B_{i2}(d) = [C_{i2} + D_{i2} \times P_1(d) + E_{i2} \times P_2(d) + F_{i2} \times P_3(d) + G_{i2} \times P_4(d)] cos(2\pi d/365.25) + [H_{i2} + I_{i2} \times P_1(d) + J_{i2} \times P_2(d) + K_{i2} \times P_3(d) + L_{i2} \times P_4(d)] sin(2\pi d/365.25) \quad (4)$$

$$B_{i3}(d) = [C_{i3} + D_{i3} \times P_1(d) + E_{i3} \times P_2(d) + F_{i3} \times P_3(d) + G_{i3} \times P_4(d)] cos(4\pi d/365.25) + [H_{i3} + I_{i3} \times P_1(d) + J_{i3} \times P_2(d) + K_{i3} \times P_3(d) + L_{i3} \times P_4(d)] sin(4\pi d/365.25) \quad (5)$$

Where $A_i(d)$ is the i-th EOF coefficient, and it can be expressed by three components, B_{i1}, B_{i2}, B_{i3}, which represent the solar cycle, annual and semi-annual variations in the EOF coefficients. For the best fits, P_1, P_2, P_3 and P_4 are the selected helio-geophysical parameters from 4 classes of helio-geophysical indices. For A_1, they are F10.7P index, Kp, Bt and E_{kl}; for A_2, they are F10.7P index, Kp, Bz and E_{kl}; for A_3, they are F10.7P index, Dst, By and E_{kl}; for A_4, they are F10.7P index, Kp, By and E_{kl}. The fitting parameters, namely C, D, E, F, G, H, I, J, K and L, can be calculated by linear regression. The regression coefficients are presented in Table 3. Using these regression coefficients, the EOF coefficients can be calculated from the selected helio-geophysical indices using equations 2)-5).

Table 3. Regression coefficients used in Equations 2)-5).

Regression coefficients	i=1	i=2	i=3	i=4
C_{i1}	-5.65	0.29	4.82	3.62
D_{i1}	0.12	0.03	-0.04	-0.02
E_{i1}	0.24	-0.18	0.01	-0.02
F_{i1}	0.40	0.76	-0.37	0.38
G_{i1}	0.83	-0.15	-0.08	-0.73
C_{i2}	-5.58	-1.63	1.72	1.69
D_{i2}	0.06	0.02	-0.01	-0.02
E_{i2}	0.04	-0.00	0.01	-0.02
F_{i2}	0.19	-0.05	-0.28	0.18
G_{i2}	-0.08	-0.19	-0.40	-0.11
H_{i2}	-0.14	0.15	-0.01	-0.13
I_{i2}	-0.00	-0.00	-0.00	0.00
J_{i2}	0.00	0.01	0.00	-0.00

K_{i2}	-0.04	-0.12	-0.06	-0.01
L_{i2}	0.12	0.02	0.01	0.06
C_{i3}	2.19	0.35	-1.34	0.25
D_{i3}	-0.04	-0.01	0.02	-0.00
E_{i3}	0.05	0.05	0.01	-0.00
F_{i3}	-0.01	-0.08	0.11	-0.12
G_{i3}	-0.04	-0.21	0.13	-0.03
H_{i3}	0.55	0.04	0.08	-0.19
I_{i3}	-0.00	-0.00	-0.00	0.00
J_{i3}	-0.01	-0.00	0.00	0.01
K_{i3}	-0.06	-0.09	0.03	0.04
L_{i3}	0.09	0.07	0.15	-0.05

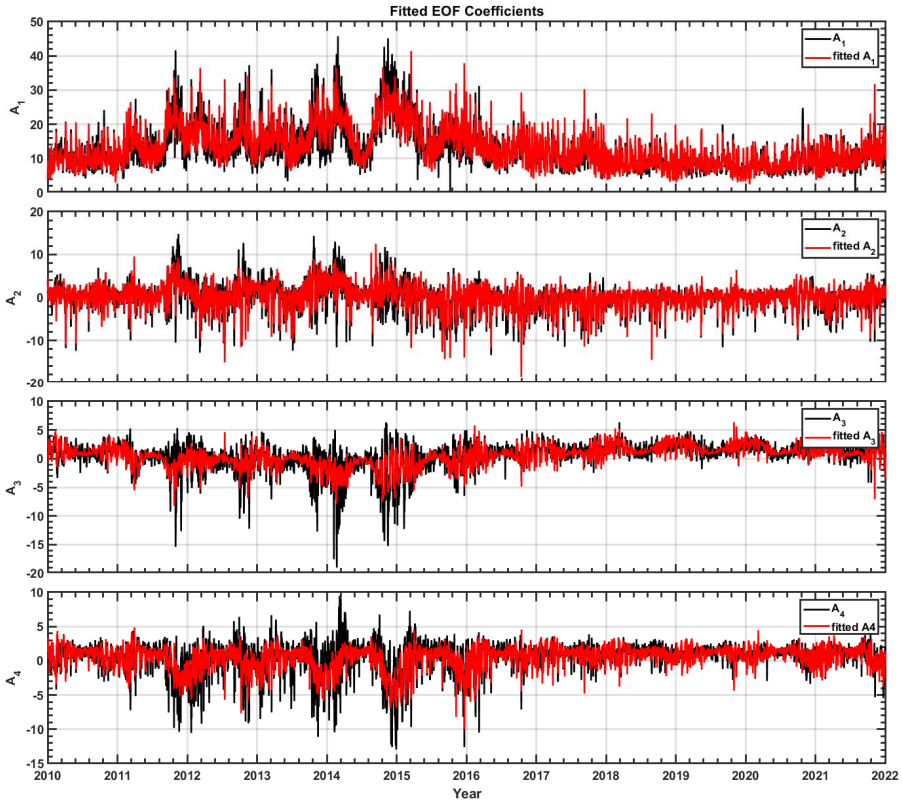

Figure 7. The EOF coefficients and the fitted coefficients using selected helio-geophysical indices.

Figure 7 shows the fits of the four EOF coefficients. The original EOF coefficients are also plotted to compare with the corresponding fits. The fits of the first two EOF coefficients agree with the original EOF coefficients very well, with only small discrepancies during high solar activity years during 2014-

2015. However, the fits of the 3rd and 4th EOF coefficients are poorer, especially during high solar activity years. Note the 3rd and 4th EOF only contains 4.5% of the total variability. Therefore, the inperfect fits will not greatly affect the overall performance of the EOF model.

3.3 Data-Model Comparison

In section 3.2, we have developed an empirical EOF model of ROTI in the Northern Hemisphere. Given the EOF base functions, the regression coefficients (C, D, E, F, G, H, I, J, K and L), and the selected helio-geophysical indices (F10.7P, Kp, Dst, Bt, By, Bz and E_{kl}), we are able to calculate the modeled ROTI map at any time. To perform a validation of the EOF model, we directly compare the modeled ROTI maps with the experimental data. Figure 8 shows the comparison between experimental ROTI data and EOF model from years 2010 to 2022. The ROTI data in years 2010-2021 are used to develop the EOF model. Thus, the comparisons in panels a)-l) stand for self-validation. The EOF model can well represent the experimental data as indicated by the high values of correlation coefficients. We also note slightly lower correlation coefficients during the high solar activity years in 2014 and 2015 (R=0.90) as compared to the lower solar activity years in 2010 (R=0.94). This can be explained by a slightly worse fit of the EOF coefficients during the high solar activity years (cf. Figure 7). This kind of behavior is opposite to the EOF modeling of other ionospheric parameters such as the F2 peak height and TEC (Zhang et al., 2009; A et al., 2012). The aggregated comparison during 2010-2021 is shown in Figure 8n, which shows a high correlation coefficient of 0.94. Figure 8o shows the histogram of the bias (Data – Model). The mean bias is 0.001 TECU/min, which indicates a very low bias. The standard deviation is 0.031 TECU/min. In order to present a cross-validation of the EOF model, we show in Figure 8m a comparison with independent data in 2022. The correlation between data and model is still high (R=0.84). This suggests that the EOF model is able to represent the climatological feature of ROTI maps for independent dataset.

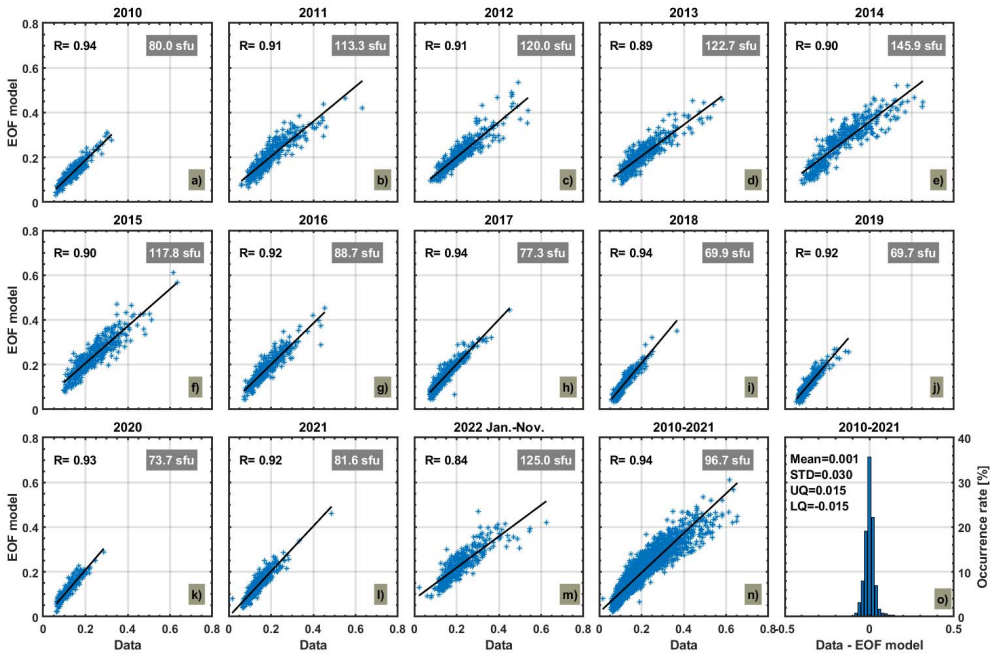

306
307
308 Figure 8. (a-n) Scatter plots to show comparisons between data and modeled results using the helio-
309 geophysical indices as input. In each scatter plot, one point is the mean value of one ROTI map at one
310 day (for both data and model). The Pearson correlation coefficient is shown on the top left of each
311 panel. The linear fits of data and modeled results are presented as a black line in each panel. The
312 average value of F10.7 index during the corresponding time period is presented on the top right of
313 each panel. Note that the data in 2022 are not used in the development of the EOF model. (o) the
314 histogram of the bias (Data – Model) in a bin-step of 0.02 TECU/min. STD = standard deviation; UQ =
315 upper quartile; LQ = lower quartile.

316 **4 Discussion**

317 In this paper, we have developed an empirical model based on the daily ROTI maps in the northern
318 mid- and high latitudes over 12 years (2010-2021). By using the EOF method, the ROTI maps are
319 decomposed into a series of base functions and corresponding coefficients. Due the rapid
320 convergence of the method, the first four EOFs can capture 96% of the total data variability. We thus
321 use the first four EOFs to construct the EOF model. By correlation analysis of the coefficients with
322 respect to various helio-geophysical indices, we select four classes of helio-geophysical parameters
323 to fit the EOF coefficients, while the EOF base functions are fixed. Given the regression coefficients (C,
324 D, E, F, G, H, I, J, K and L in Table 3) and the selected helio-geophysical indices (F10.7P, Kp, Dst, Bt, By,
325 Bz and E_{kl}), the EOF model can predict the ROTI map at any given time. The data-model comparison
326 in section 3.3 gives satisfactory results and high correlation coefficient. Note that the good

performance of the EOF model is on the climatological scale. We also note that the correlation between data and model is slightly lower during high solar activity (cf. Figure 8). This might be expected, as the validation of the International Reference Ionosphere (IRI) also indicates that empirical model tends to poorly represent the variability of high-latitude ionosphere during high solar activity (Themens & Jayachandran, 2016; Bjoland et al., 2016). This has been attributed to the high sensitivity to geomagnetic conditions and highly nonlinear dynamics (Themens et al., 2018).

The advantage of the EOF model is that it can decompose the data variability into different categories. Different helio-geophysical indices represent different drivers/sources of ionospheric plasma irregularities. For example, the first EOF represents the average behavior of the ROTI activity, and it is positively correlated with F10.7P, the geomagnetic activity and the IMF strength. The second EOF mainly represents the latitudinal variations as well as the expansion and contraction of the ROTI activity. There is a high correlation between the second EOF coefficient versus Kp and IMF Bz. For example, during negative IMF Bz, the auroral oval and ionospheric plasma irregularities can expand to lower latitudes (Li et al., 2010; Alfonsi et al., 2011; Jin et al., 2020; Cherniak & Zakharenkova, 2017). The 3rd and 4th EOFs represent the dawn-dusk asymmetry. These two components are related to the IMF By which modulates ionospheric convection pattern at high latitudes (e.g., Weimer, 2005). This feature is also consistent with the IMF By dependence of the polar cap patches and ionospheric plasma irregularities at high latitudes (Spicher et al., 2017; Jin et al., 2019b).

The EOF model only depends on seven helio-geophysical indices (F10.7P, Kp, Dst, Bt, By, Bz and E_{kl}). These helio-geophysical indices reflect different helio-geophysical drivers/sources (i.e., solar activity, geomagnetic storms, IMF and solar wind) of irregularities in the high-latitude ionosphere. A number of different helio-geophysical indices have been used to develop space weather models in the literature. For example, Fabbro et al. (2021) developed a ROTI model by using the Newell coupling function as a driver to parameterize the lognormal distribution of ROTI. The model is able to forecast the probability of ROTI that exceeds a given threshold. We also note that Fabbro et al. (2021) used ROTI based on 1-s resolution data, whilst we use ROTI data based on 30-s resolution data. The calculation of ROTI using different resolution may result in different level of activity (Jacobsen, 2014). However, one major difference in the methodology from our model is that the model does not take into account of the variations that are related to the general level of the solar EUV radiation. A climatological model must take such variations into account. As shown in section 3.1, the global ROTI activity is greatly affected by the solar activity that can be characterized by F10.7P. The solar EUV radiation is the major source of the background ionospheric density even for the polar ionosphere (Moen et al., 2008; Yang et al., 2016; Jin & Xiong, 2020). During the solar maximum, a small percentage of perturbations in the high background electron density would produce significant ROTI

and scintillations (Aarons et al., 1981; Basu et al., 1988; Jin et al., 2018). In order to forecast ROTI activity across different levels of solar activity, it is necessary to use indices that represent the solar activity. In our model, we use F10.7P, and this allows us to forecast ROTI more accurately over different phases of a solar cycle. The high-latitude ionosphere is a highly dynamic system with energy inputs from a variety of space sources. In order to resolve the complexity of the system, there are also studies that use as many helio-geophysical indices as possible. For example, McGranaghan et al. (2018) used 51 helio-geophysical parameters to predict the high-latitude GNSS phase scintillation. In our study, we try to balance the simplicity and accuracy of the model by using information only from the major sources/drivers to describe the system. We thus include four classes of major drivers and the selection of indices is done according to the correlation analysis and physical meaning. The simplicity of our model ensures the robustness and makes it easy to implement and use for general users.

We are aware that our newly developed EOF model is a climatological model, which represents the ROTI activity during relative quiet time. Though it is not designed for disturbed conditions, we next show the worst scenario during very disturbed condition. The St. Patrick's Day storm in 2015 is the strongest storm in solar cycle 24 (Kamide & Kusano, 2015; Jacobsen & Andalsvik, 2016; Cherniak et al., 2015; Astafyeva et al., 2015). The minimum Dst reached −223 nT on March 17, 2015. Figures 9a-9c present the IGS ROTI maps before and during the magnetic storm, while Figures 9d-9f show the modeled results for the same time. The EOF model gives a quite consistent prediction of the ROTI observations before the storm on March 16. There was one enhancement from noon to dusk and 76°-82° MLAT. However, the ROTI observations and the modeled results are quite different (especially on the dayside) during the main phase (March 17) of the storm. On March 17, the area of high ROTI is greatly expanded as a result of the expanded auroral oval (Prikryl et al., 2016; Jin & Oksavik, 2018). In addition, the enhancement of ROTI associated with storm-enhanced density (SED) at mid-latitudes (15-18 MLT, 50°-60° MLAT) is not reflected by the EOF model. The transport of polar cap patches and TOI across the polar cap is well captured by the EOF model. On March 18 (recovery phase), the EOF model is more consistent with the IGS ROTI map except for an area of enhancement around 13-14 MLT and 60°-70° MLAT in Figure 9c. The ROTI enhancement near the dayside and duskside auroral oval is well reproduced by the EOF model.

The inadequate prediction during strong storms can be partly attributed to fixed EOF base functions. In our model, only the EOF coefficients are adjusted by helio-geophysical parameters as inputs, while the EOF base functions stay fixed. This means that the helio-geophysical indices can only modulate the contribution (intensity) of each base function by changing the corresponding EOF coefficients. For example, the first base function E_1 represents the average behavior of the high-latitude ROTI. The

enhancement on the dayside is around 10-15 MLT and 75°-80° MLAT, while it is located around 21-02 MLT and 68°-74° MLAT on the nightside (cf. Figure 6a). The second base function E_2 represents the impact of IMF Bz and geomagnetic activity. There is a ring of depletion of E_2, i.e., 70°-76° MLAT around noon and 60°-70° MLAT on the nightside (cf. Figure 6b). This component can reflect the expansion of the auroral activity due to negative IMF Bz. However, the most significant expansion during major geomagnetic storms can only be partly modeled by the second EOF (E_2 and A_2), i.e., the equatorward expansion to 70° MLAT around noon and 60° MLAT on the nightside. However, during the severe geomagnetic storm on March 17, 2015, enhanced ROTI expanded to as low as 62° MLAT around noon (Figure 9b). In addition, enhanced ROTI associated with the SED is not captured by any of the EOF base functions. This suggests that severe geomagnetic storms, such as the one on March 17, 2015, cannot be represented fully by the EOF model.

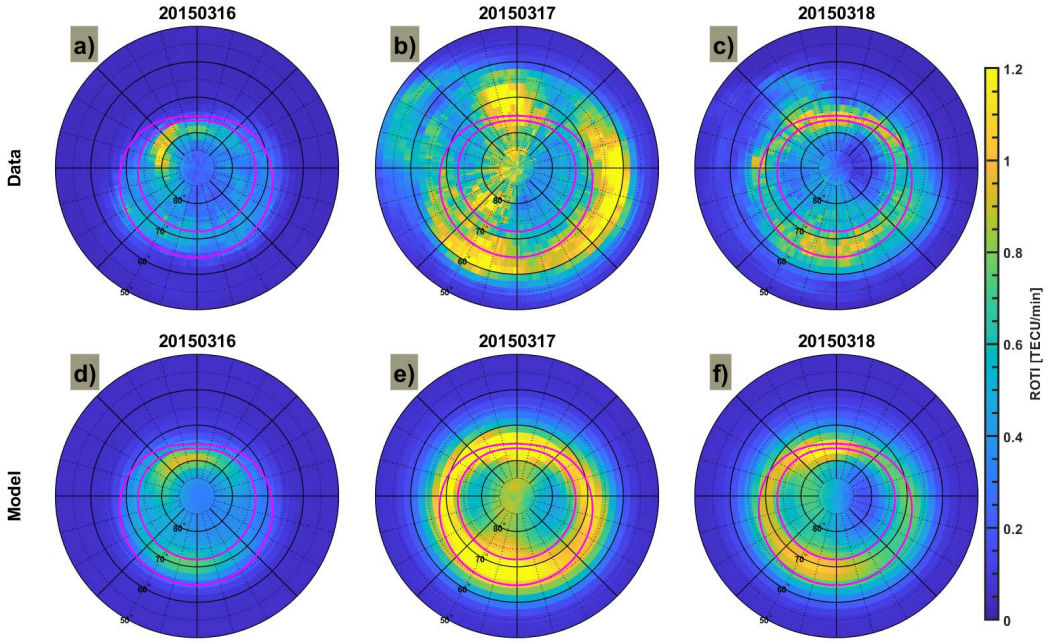

Figure 9. The comparison of IGS ROTI maps (top) and ROTI maps calculated using the EOF model (bottom) before and during the St. Patrick Day storm in 2015. In each panel, noon is to the top, and dawn is to the right.

One straightforward way to improve the model performance during severe geomagnetic storms is to build a storm model based on data during storms. For example, it is possible to make a correction model that can adjust the quiet time model to account for storm-time variability (Araujo-Pradere et al., 2002; Themens et al., 2018). The most obvious difference between the model and observations is the significant expansion of the dayside ROTI region. To overcome this drawback, one can make the

second EOF base function E_2 to be driven by the IMF Bz as well, in order to account for the significant expansion of auroral oval during great storms. In such a way, the IMF Bz and geomagnetic activity not only modulate the amplitude but also the location of ROTI. Another phenomenon that is not captured in our model is the mid-latitude SED. It is necessary to build a new model for SED as an adjustment to the current model. These methods and possibilities will be explored in future studies.

5. Summary and conclusion

In this study, we have constructed an empirical model based on the daily ROTI maps in the Northern Hemisphere over 12 years (2010-2021). We first presented the long-term climatology of TEC irregularities from the IGS ROTI maps (section 3.1). The ROTI maps were derived using 30-s resolution GNSS data from worldwide GNSS stations (about 700 stations). The global distribution of used GNSS stations ensures that the ROTI data should have a very little longitudinal effect or universal time dependence. This is a great advantage over previous models that often use regional data from the European or American sectors. The 2-D ROTI maps show a variety of spatial and temporal variability. The most obvious variation is the solar activity dependence, and this variability can be well characterized by the F10.7P index. The seasonal variations are also clear, i.e., ROTI is more enhanced during winter as compared to summer. The seasonal variations can be explained by the balance of the energy input into the polar ionosphere and the solar illumination that creates E region conductance and damps the amplitude of ionospheric irregularities. The diurnal variations (with respect to MLT) are also observed such that enhanced ROTI is observed from noon to dusk on the dayside, and around magnetic midnight. The latitudinal scan of ROTI along the noon-midnight meridian can also reveal some key features of ionospheric irregularities. For example, the region of enhanced ROTI around noon shows oscillations over a period of one year. This feature has been explained by the seasonal shift of the cusp and the impact of the solar terminator.

By applying the EOF method, the ROTI maps are decomposed into a series of base functions and corresponding coefficients. Due to the fast convergence, the first four EOFs capture 96% of the total data variability. We use the first four EOFs to build the EOF model. The first EOF is the dominant component that represents the averaged picture of ROTI activity. The first EOF is mostly determined by the solar activity and geomagnetic activity. The second EOF reflects an important deviation (4.43% of total data variability) from the averaged ROTI activity, and it represents the impacts of geomagnetic activity and IMF. More specifically, it can reflect the equatorward expansion of ROTI activity during moderate southward turn of IMF Bz. The third and fourth EOFs reflect the dawn-dusk asymmetry that is modulated by IMF By.

By correlation analysis of the EOF coefficients with respect to various helio-geophysical indices, we choose four classes of helio-geophysical parameters to fit the EOF coefficients, while the EOF base functions remain fixed. The final EOF model is only dependent on seven selected helio-geophysical indices (F10.7P, Kp, Dst, Bt, By, Bz and E_{kl}). Given the seven selected helio-geophysical indices, the EOF model is capable to make prediction of ROTI maps at any time. The data-model comparison gives satisfactory results and high correlation coefficient (Pearson correlation coefficient of 0.94). The validation with data in 2022 outside of the model training dataset also gives satisfactory result (R = 0.84).

Note that the good performance of the EOF model is related to the quiet time in a climatological sense. We have also presented a data-model comparison during the St. Patrick's Day storm in 2015. During this severe geomagnetic storm, enhanced ROTI associated with mid-latitude SED and great equatorward expansion of enhanced ROTI to as low as 62° MLAT around noon is not captured by the EOF model. Future effort is needed to provide supplemental adjustments/corrections to the climatological model to account for severe storms.

In this study, we have expanded our previous work about 1-D EOF model using a single station to a 2-D EOF model of ROTI irregularities over the entire Arctic area. Due to the long-term datasets and global distribution of GNSS stations, this new model should be applicable to the whole Arctic. The EOF model is only dependent on 7 commonly used helio-geophysical indices, and thus it is simple to implement and use. It is also possible to develop models that are dependent on fewer helio-geophysical parameters, in order to accommodate the scenario when some indices are not available at times. However, to ensure an adequate performance, the simplified models should at least include F10.7, geomagnetic activity and IMF. This study demonstrates that the EOF method is very suitable and efficient for developing models for ionospheric irregularities. The EOF method is very straightforward and it can also be applied to other irregularity indices, such as the GNSS amplitude and phase scintillation indices from ground-based GNSS scintillation receivers, as well as in-situ irregularity indices obtained from Low Earth Orbiting satellites (Jin et al., 2022b; Kotova et al., 2022).

Acknowledgment

WJM, YJ and DK acknowledge funding from the European Research Council (ERC) under the European Union's Horizon 2020 research and innovation programme (ERC Consolidator Grant agreement No. 866357, POLAR-4DSpace). This research is a part of the 4DSpace Strategic Research Initiative at the University of Oslo and the European Space Agency's network of space weather services and service development activities, supported under ESA contract number 4000139062/22/D/KS.

Open Research

The ROTI maps can be obtained from the ftp server of NASA's Crustal Dynamics Data Information System (CDDIS) https://cddis.nasa.gov/archive/gnss/products/ionex/. The helio-geophysical indices can be obtained through https://omniweb.gsfc.nasa.gov/form/dx1.html.

References

A, E., Zhang, D., Ridley, A. J., Xiao, Z., & Hao, Y. (2012). A global model: Empirical orthogonal function analysis of total electron content 1999–2009 data. *Journal of Geophysical Research: Space Physics, 117*(A3). doi:https://doi.org/10.1029/2011JA017238

A, E., Zhang, D. H., Xiao, Z., Hao, Y. Q., Ridley, A. J., & Moldwin, M. (2011). Modeling ionospheric foF2 by using empirical orthogonal function analysis. *Ann. Geophys., 29*(8), 1501-1515. doi:10.5194/angeo-29-1501-2011

Alfonsi, L., Spogli, L., De Franceschi, G., Romano, V., Aquino, M., Dodson, A., & Mitchell, C. N. (2011). Bipolar climatology of GPS ionospheric scintillation at solar minimum. *Radio Science, 46*. doi:10.1029/2010rs004571

Araujo-Pradere, E. A., Fuller-Rowell, T. J., & Codrescu, M. V. (2002). STORM: An empirical storm-time ionospheric correction model - 1. Model description. *Radio Science, 37*(5). doi:10.1029/2001rs002467

Astafyeva, E., Zakharenkova, I., & Forster, M. (2015). Ionospheric response to the 2015 St. Patrick's Day storm: A global multi-instrumental overview. *Journal of Geophysical Research-Space Physics, 120*(10), 9023-9037. doi:10.1002/2015ja021629

Basu, S., Basu, S., Mackenzie, E., Coley, W. R., Sharber, J. R., & Hoegy, W. R. (1990). Plasma Structuring by the Gradient Drift Instability at High-Latitudes and Comparison With Velocity Shear Driven Processes. *Journal of Geophysical Research-Space Physics, 95*(A6), 7799-+. doi:10.1029/JA095iA06p07799

Basu, S., Groves, K. M., Basu, S., & Sultan, P. J. (2002). Specification and forecasting of scintillations in communication/navigation links: current status and future plans. *Journal of Atmospheric and Solar-Terrestrial Physics, 64*(16), 1745-1754. doi:10.1016/s1364-6826(02)00124-4

Basu, S., Groves, K. M., Quinn, J. M., & Doherty, P. (1999). A comparison of TEC fluctuations and scintillations at Ascension Island. *Journal of Atmospheric and Solar-Terrestrial Physics, 61*(16), 1219-1226. doi:Doi 10.1016/S1364-6826(99)00052-8

Basu, S., Mackenzie, E., & Basu, S. (1988). Ionospheric Constraints on VHF UHF Communications Links during Solar Maximum and Minimum Periods. *Radio Science, 23*(3), 363-378. doi:DOI 10.1029/RS023i003p00363

Bilitza, D., McKinnell, L.-A., Reinisch, B., & Fuller-Rowell, T. (2011). The international reference ionosphere today and in the future. *Journal of Geodesy, 85*(12), 909-920. doi:10.1007/s00190-010-0427-x

Bjoland, L. M., Belyey, V., Løvhaug, U. P., & La Hoz, C. (2016). An evaluation of International Reference Ionosphere electron density in the polar cap and cusp using EISCAT Svalbard radar measurements. *Ann. Geophys., 34*(9), 751-758. doi:10.5194/angeo-34-751-2016

Cherniak, I., Krankowski, A., & Zakharenkova, I. (2014). Observation of the ionospheric irregularities over the Northern Hemisphere: Methodology and service. *Radio Science, 49*(8), 653-662. doi:https://doi.org/10.1002/2014RS005433

Cherniak, I., Krankowski, A., & Zakharenkova, I. (2018a). ROTI Maps: a new IGS ionospheric product characterizing the ionospheric irregularities occurrence. *Gps Solutions, 22*(3), 69. doi:10.1007/s10291-018-0730-1

Cherniak, I., Krankowski, A., & Zakharenkova, I. (2018b). ROTI Maps: a new IGS ionospheric product characterizing the ionospheric irregularities occurrence. *Gps Solutions, 22*(3). doi:10.1007/s10291-018-0730-1

Cherniak, I., & Zakharenkova, I. (2017). New advantages of the combined GPS and GLONASS observations for high-latitude ionospheric irregularities monitoring: case study of June 2015 geomagnetic storm. *Earth Planets and Space, 69*. doi:10.1186/s40623-017-0652-0

Cherniak, I., Zakharenkova, I., & Redmon, R. J. (2015). Dynamics of the high-latitude ionospheric irregularities during the 17 March 2015St. Patrick's Day storm: Ground-based GPS measurements. *Space Weather-the International Journal of Research and Applications, 13*(9), 585-597. doi:10.1002/2015sw001237

Coley, W. R., & Heelis, R. A. (1998). Structure and occurrence of polar ionization patches. *Journal of Geophysical Research-Space Physics, 103*(A2), 2201-2208. doi:10.1029/97ja03345

Cowley, S. W. H., & Lockwood, M. (1992). Excitation and Decay of Solar Wind-Driven Flows in the Magnetosphere-Ionosphere System. *Annales Geophysicae-Atmospheres Hydrospheres and Space Sciences, 10*(1-2), 103-115. Retrieved from <Go to ISI>://WOS:A1992HL02700010

De Franceschi, G., Spogli, L., Alfonsi, L., Romano, V., Cesaroni, C., & Hunstad, I. (2019). The ionospheric irregularities climatology over Svalbard from solar cycle 23. *Scientific Reports, 9*. doi:10.1038/s41598-019-44829-5

Dvinskikh, N. I., & Naidenova, N. I. (1991). An adaptable regional empirical ionospheric model. *Advances in Space Research, 11*, 7. doi:10.1016/0273-1177(91)90312-8

Fabbro, V., Jacobsen, K. S., Andalsvik, Y. L., & Rougerie, S. (2021). GNSS positioning error forecasting in the Arctic: ROTI and Precise Point Positioning error forecasting from solar wind measurements. *J. Space Weather Space Clim., 11*, 43. Retrieved from https://doi.org/10.1051/swsc/2021024

Foster, J. C., Coster, A. J., Erickson, P. J., Holt, J. M., Lind, F. D., Rideout, W., . . . Rich, F. J. (2005). Multiradar observations of the polar tongue of ionization. *Journal of Geophysical Research-Space Physics, 110*(A9). doi:10.1029/2004ja010928

Holzworth, R. H., & Meng, C. I. (1975). Mathematical Representation of Auroral Oval. *Geophysical Research Letters, 2*(9), 377-380. doi:DOI 10.1029/GL002i009p00377

Jacobsen, K. S. (2014). The impact of different sampling rates and calculation time intervals on ROTI values. *J. Space Weather Space Clim., 4*, A33. Retrieved from https://doi.org/10.1051/swsc/2014031

Jacobsen, K. S., & Andalsvik, Y. L. (2016). Overview of the 2015 St. Patrick's day storm and its consequences for RTK and PPP positioning in Norway. *J. Space Weather Space Clim., 6*, A9. Retrieved from https://doi.org/10.1051/swsc/2016004

Jacobsen, K. S., & Dahnn, M. (2014). Statistics of ionospheric disturbances and their correlation with GNSS positioning errors at high latitudes. *Journal of Space Weather and Space Climate, 4*(A27). doi:10.1051/swsc/2014024

Jakowski, N., Beniguel, Y., De Franceschi, G., Pajares, M. H., Jacobsen, K. S., Stanislawska, I., . . . Wautelet, G. (2012). Monitoring, tracking and forecasting ionospheric perturbations using GNSS techniques. *Journal of Space Weather and Space Climate, 2*, 14. doi:10.1051/swsc/2012022

Jin, Y., Clausen, L. B. N., Miloch, W. J., Høeg, P., Jarmołowski, W., Wielgosz, P., . . . García-Rigo, A. (2022a). Climatology and modeling of ionospheric irregularities over Greenland based on empirical orthogonal function method. *J. Space Weather Space Clim., 12*, 23. Retrieved from https://doi.org/10.1051/swsc/2022022

Jin, Y., Clausen, L. B. N., Spicher, A., Ivarsen, M. F., Zhang, Y., Miloch, W. J., & Moen, J. I. (2021). Statistical Distribution of Decameter Scale (50 m) Ionospheric Irregularities at High Latitudes. *Geophysical Research Letters, 48*(19), e2021GL094794. doi:https://doi.org/10.1029/2021GL094794

Jin, Y., Kotova, D., Xiong, C., Brask, S. M., Clausen, L. B. N., Kervalishvili, G., . . . Miloch, W. J. (2022b). Ionospheric Plasma IRregularities - IPIR - Data Product Based on Data From the Swarm

Satellites. *Journal of Geophysical Research: Space Physics, 127*(4), e2021JA030183. doi:https://doi.org/10.1029/2021JA030183

Jin, Y., Moen, J. I., Spicher, A., Oksavik, K., Miloch, W. J., Clausen, L. B. N., . . . Saito, Y. (2019a). Simultaneous Rocket and Scintillation Observations of Plasma Irregularities Associated With a Reversed Flow Event in the Cusp Ionosphere. *Journal of Geophysical Research: Space Physics, 124*(8), 7098-7111. doi:10.1029/2019ja026942

Jin, Y., & Xiong, C. (2020). Interhemispheric Asymmetry of Large-Scale Electron Density Gradients in the Polar Cap Ionosphere: UT and Seasonal Variations. *Journal of Geophysical Research: Space Physics, 125*(2), e2019JA027601. doi:10.1029/2019ja027601

Jin, Y., Xiong, C., Clausen, L., Spicher, A., Kotova, D., Brask, S., . . . Miloch, W. (2020). Ionospheric Plasma Irregularities Based on In Situ Measurements From the Swarm Satellites. *Journal of Geophysical Research: Space Physics, 125*(7), e2020JA028103. doi:https://doi.org/10.1029/2020JA028103

Jin, Y. Q., Miloch, W. J., Moen, J. I., & Clausen, L. B. N. (2018). Solar cycle and seasonal variations of the GPS phase scintillation at high latitudes. *Journal of Space Weather and Space Climate, 8*. doi:10.1051/swsc/2018034

Jin, Y. Q., Moen, J. I., & Miloch, W. J. (2014). GPS scintillation effects associated with polar cap patches and substorm auroral activity: direct comparison. *Journal of Space Weather and Space Climate, 4*(A23). doi:10.1051/swsc/2014019

Jin, Y. Q., Moen, J. I., & Miloch, W. J. (2015). On the collocation of the cusp aurora and the GPS phase scintillation: A statistical study. *Journal of Geophysical Research-Space Physics, 120*(10), 9176-9191. doi:10.1002/2015ja021449

Jin, Y. Q., & Oksavik, K. (2018). GPS Scintillations and Losses of Signal Lock at High Latitudes During the 2015 St. Patrick's Day Storm. *Journal of Geophysical Research-Space Physics, 123*(9), 7943-7957. doi:10.1029/2018ja025933

Jin, Y. Q., Spicher, A., Xiong, C., Clausen, L. B. N., Kervalishvili, G., Stolle, C., & Miloch, W. J. (2019b). Ionospheric Plasma Irregularities Characterized by the Swarm Satellites: Statistics at High Latitudes. *Journal of Geophysical Research-Space Physics, 124*(2), 1262-1282. doi:10.1029/2018ja026063

Kamide, Y., & Kusano, K. (2015). No Major Solar Flares but the Largest Geomagnetic Storm in the Present Solar Cycle. *Space Weather-the International Journal of Research and Applications, 13*(6), 365-367. doi:https://doi.org/10.1002/2015SW001213

Kan, J., & Lee, L. (1979). Energy coupling function and solar wind-magnetosphere dynamo. *Geophysical Research Letters, 6*(7), 577-580.

King, J. H., & Papitashvili, N. E. (2005). Solar wind spatial scales in and comparisons of hourly Wind and ACE plasma and magnetic field data. *Journal of Geophysical Research-Space Physics, 110*(A2). doi:10.1029/2004ja010649

Kintner, P. M., Ledvina, B. M., & De Paula, E. R. (2007). GPS and ionospheric scintillations. *Space Weather-the International Journal of Research and Applications, 5*(9). doi:10.1029/2006sw000260

Kotova, D., Jin, Y., Spogli, L., Wood, A. G., Urbar, J., Rawlings, J. T., . . . Miloch, W. J. (2022). Electron density fluctuations from Swarm as a proxy for ground-based scintillation data: A statistical perspective. *Advances in Space Research*. doi:https://doi.org/10.1016/j.asr.2022.11.042

Kotulak, K., Zakharenkova, I., Krankowski, A., Cherniak, I., Wang, N., & Fron, A. (2020). Climatology Characteristics of Ionospheric Irregularities Described with GNSS ROTI. *Remote Sensing, 12*(16), 2634. Retrieved from https://www.mdpi.com/2072-4292/12/16/2634

Li, G. Z., Ning, B. Q., Ren, Z. P., & Hu, L. H. (2010). Statistics of GPS ionospheric scintillation and irregularities over polar regions at solar minimum. *Gps Solutions, 14*(4), 331-341. doi:10.1007/s10291-009-0156-x

Liu, L., Wan, W., Chen, Y., & Le, H. (2011). Solar activity effects of the ionosphere: A brief review. *Chinese Science Bulletin, 56*(12), 1202-1211. doi:10.1007/s11434-010-4226-9

Lockwood, M., Cowley, S. W. H., & Freeman, M. P. (1990). The Excitation of Plasma Convection in the High-Latitude Ionosphere. *Journal of Geophysical Research-Space Physics, 95*(A6), 7961-7972. doi:DOI 10.1029/JA095iA06p07961

McGranaghan, R. M., Mannucci, A. J., Wilson, B., Mattmann, C. A., & Chadwick, R. (2018). New Capabilities for Prediction of High-Latitude Ionospheric Scintillation: A Novel Approach With Machine Learning. *Space Weather-the International Journal of Research and Applications, 16*(11), 1817-1846. doi:https://doi.org/10.1029/2018SW002018

Mitchell, C. N., Alfonsi, L., De Franceschi, G., Lester, M., Romano, V., & Wernik, A. W. (2005). GPS TEC and scintillation measurements from the polar ionosphere during the October 2003 storm. *Geophysical Research Letters, 32*(12). doi:10.1029/2004gl021644

Moen, J., Oksavik, K., Abe, T., Lester, M., Saito, Y., Bekkeng, T. A., & Jacobsen, K. S. (2012). First in-situ measurements of HF radar echoing targets. *Geophysical Research Letters, 39*. doi:10.1029/2012gl051407

Moen, J., Qiu, X. C., Carlson, H. C., Fujii, R., & McCrea, I. W. (2008). On the diurnal variability in F2-region plasma density above the EISCAT Svalbard radar. *Annales Geophysicae, 26*(8), 2427-2433. doi:DOI 10.5194/angeo-26-2427-2008

Newell, P. T., & Meng, C. I. (1989). Dipole Tilt Angle Effects on the Latitude of the Cusp and Cleft Low-Latitude Boundary-Layer. *Journal of Geophysical Research-Space Physics, 94*(A6), 6949-6953. doi:DOI 10.1029/JA094iA06p06949

Newell, P. T., Sotirelis, T., Liou, K., Meng, C. I., & Rich, F. J. (2007). A nearly universal solar wind-magnetosphere coupling function inferred from 10 magnetospheric state variables. *Journal of Geophysical Research-Space Physics, 112*(A1). doi:10.1029/2006ja012015

Pi, X., Mannucci, A. J., Lindqwister, U. J., & Ho, C. M. (1997). Monitoring of global ionospheric irregularities using the worldwide GPS network. *Geophysical Research Letters, 24*(18), 2283-2286. doi:10.1029/97gl02273

Prikryl, P., Ghoddousi-Fard, R., Weygand, J. M., Viljanen, A., Connors, M., Danskin, D. W., . . . Sreeja, V. (2016). GPS phase scintillation at high latitudes during the geomagnetic storm of 17–18 March 2015. *Journal of Geophysical Research: Space Physics, 121*(10), 10,448-410,465. doi:10.1002/2016ja023171

Priyadarshi, S. (2015). A Review of Ionospheric Scintillation Models. *Surveys in Geophysics, 36*(2), 295-324. doi:10.1007/s10712-015-9319-1

Rentz, S., & Lühr, H. (2008). *Climatology of the cusp-related thermospheric mass density anomaly, as derived from CHAMP observations.* Annales Geophysicae, pp. 2807-2823.

Rino, C. L., Livingston, R. C., Tsunoda, R. T., Robinson, R. M., Vickrey, J. F., Senior, C., . . . Klobuchar, J. A. (1983). Recent Studies of the Structure and Morphology of Auroral-Zone F-Region Irregularities. *Radio Science, 18*(6), 1167-1180. doi:DOI 10.1029/RS018i006p01167

Secan, J. A., Bussey, R. M., Fremouw, E. J., & Basu, S. (1997). High-latitude upgrade to the Wideband ionospheric scintillation model. *Radio Science, 32*(4), 1567-1574. doi:https://doi.org/10.1029/97RS00453

Spicher, A., Clausen, L. B. N., Miloch, W. J., Lofstad, V., Jin, Y., & Moen, J. I. (2017). Interhemispheric study of polar cap patch occurrence based on Swarm in situ data. *Journal of Geophysical Research-Space Physics, 122*(3), 3837-3851. doi:10.1002/2016ja023750

Spogli, L., Alfonsi, L., De Franceschi, G., Romano, V., Aquino, M. H. O., & Dodson, A. (2009). Climatology of GPS ionospheric scintillations over high and mid-latitude European regions. *Annales Geophysicae, 27*(9), 3429-3437. doi:DOI 10.5194/angeo-27-3429-2009

Tapping, K. F. (2013). The 10.7 cm solar radio flux (F10.7). *Space Weather-the International Journal of Research and Applications, 11*(7), 394-406. doi:10.1002/swe.20064

Themens, D. R., & Jayachandran, P. T. (2016). Solar activity variability in the IRI at high latitudes: Comparisons with GPS total electron content. *Journal of Geophysical Research-Space Physics, 121*(4), 3793-3807. doi:10.1002/2016ja022664

Themens, D. R., Jayachandran, P. T., Reid, B., & McCaffrey, A. M. (2018). The Limits of Empirical Electron Density Modeling: Examining the Capacity of E-CHAIM and the IRI for Modeling

679 Intermediate (1- to 30-Day) Timescales at High Latitudes. *Radio Science, 55*(4),
680 e2018RS006763. doi:https://doi.org/10.1029/2018RS006763
681 Tsunoda, R. T. (1988). High-Latitude F-Region Irregularities - a Review and Synthesis. *Reviews of*
682 *Geophysics, 26*(4), 719-760. doi:DOI 10.1029/RG026i004p00719
683 van der Meeren, C., Oksavik, K., Lorentzen, D., Moen, J. I., & Romano, V. (2014). GPS scintillation and
684 irregularities at the front of an ionization tongue in the nightside polar ionosphere. *Journal of*
685 *Geophysical Research: Space Physics, 119*(10), 8624-8636. doi:10.1002/2014ja020114
686 Van Dierendonck, A. J., Klobuchar, J., & Hua, Q. (1993). *Ionospheric Scintillation Monitoring Using*
687 *Commercial Single Frequency C/A Code Receivers.* Proceedings of the 6th International
688 Technical Meeting of the Satellite Division of The Institute of Navigation (ION GPS 1993), Salt
689 Lake City, UT, September 1993, September 1993, pp. 1333 - 1342.
690 Weimer, D. R. (2005). Improved ionospheric electrodynamic models and application to calculating
691 Joule heating rates. *Journal of Geophysical Research-Space Physics, 110*(A5).
692 doi:10.1029/2004ja010884
693 Wernik, A. W., Alfonsi, L., & Materassi, M. (2007). Scintillation modeling using in situ data. *Radio*
694 *Science, 42*(1). doi:https://doi.org/10.1029/2006RS003512
695 Xiong, C., Park, J., Luehr, H., Stolle, C., & Ma, S. Y. (2010). Comparing plasma bubble occurrence rates
696 at CHAMP and GRACE altitudes during high and low solar activity. *Annales Geophysicae,*
697 *28*(9), 1647-1658. doi:10.5194/angeo-28-1647-2010
698 Yang, S. G., Zhang, B. C., Fang, H. X., Kamide, Y., Li, C. Y., Liu, J. M., . . . Hu, H. Q. (2016). New evidence
699 of dayside plasma transportation over the polar cap to the prevailing dawn sector in the
700 polar upper atmosphere for solar-maximum winter. *Journal of Geophysical Research-Space*
701 *Physics, 121*(6), 5626-5638. doi:10.1002/2015ja022171
702 Zhang, M. L., Liu, C., Wan, W., Liu, L., & Ning, B. (2009). A global model of the ionospheric F2 peak
703 height based on EOF analysis. *Ann. Geophys., 27*(8), 3203-3212. doi:10.5194/angeo-27-3203-
704 2009
705 Zhang, Q. H., Lockwood, M., Foster, J. C., Zhang, S. R., Zhang, B. C., McCrea, I. W., . . . Ruohoniemi, J.
706 M. (2015). Direct observations of the full Dungey convection cycle in the polar ionosphere for
707 southward interplanetary magnetic field conditions. *Journal of Geophysical Research-Space*
708 *Physics, 120*(6), 4519-4530. doi:10.1002/2015ja021172
709 Aarons, J., Mullen, J. P., Whitney, H. E., Johnson, A. L., & Weber, E. J. (1981). Uhf Scintillation Activity
710 over Polar Latitudes. *Geophysical Research Letters, 8*(3), 277-280. doi:DOI
711 10.1029/GL008i003p00277

712